REPORT DOCUMENTATION PAGE

AFRL-SR-BL-TR-01-

0157

1. REPORT DATE (DD-MM-YYYY)	2. REPORT TYPE	3. DATES COVERED (From - To)
01/26/2000	Final Technical	07/15/1997 - 06/30/2000

4. TITLE AND SUBTITLE
Distributed Turbulent Flow Control by MEMS Integrated with Neural Networks

5a. CONTRACT NUMBER

5b. GRANT NUMBER
F49620-97-0514

5c. PROGRAM ELEMENT NUMBER

6. AUTHOR(S)
Chih-Ming Ho, John Kim, Yu-Chong Tai and Rod Goodman

5d. PROJECT NUMBER
F118

5e. TASK NUMBER
09

5f. WORK UNIT NUMBER

7. PERFORMING ORGANIZATION NAME(S) AND ADDRESS(ES)
University of California, Los Angeles
10920 Wilshire Boulevard, Suite 1200
Los Angeles, CA 90024-1406

8. PERFORMING ORGANIZATION REPORT NUMBER

9. SPONSORING / MONITORING AGENCY NAME(S) AND ADDRESS(ES)
Air Force Office of Scientific Research
801 N. Randolph Street, Room 732
Arlington, VA 22203-1977

10. SPONSOR/MONITOR'S ACRONYM(S)
AFOSR/NA

11. SPONSOR/MONITOR'S REPORT NUMBER(S)

12. DISTRIBUTION / AVAILABILITY STATEMENT
Approved for public release; distribution unlimited.

13. SUPPLEMENTARY NOTES

14. ABSTRACT
We have developed new fabrication techniques that can allow the formerly incompatible CMOS and MEMS devices to be integrated onto a single chip. This achievement leads to the M^3 system, which consists of monolithically integrated sensor-logics-actuator. The M^3 system can be used to control the wall streaks in a turbulent boundary. Experimentation work revealed and solved many of the problems associated with having electronic devices work in close proximity with each other and is progressing on the efforts to develop a control system using a neural network logic. Implementation of the network as well as a more general, fully adaptive neural network onto electronic circuitry has been accomplished. Finally, CFD studies have been performed which reveals and explains the mechanisms at work in the interaction between an oscillating flap and the turbulent boundary layer.

15. SUBJECT TERMS
MEMS, flow control, turbulent boundary layer, CFD, neural networks

16. SECURITY CLASSIFICATION OF:			17. LIMITATION OF ABSTRACT	18. NUMBER OF PAGES	19a. NAME OF RESPONSIBLE PERSON
a. REPORT	b. ABSTRACT	c. THIS PAGE			Chih-Ming Ho
unclassified	unclassified	unclassified	Unlimited	24	19b. TELEPHONE NUMBER (include area code) 310-825-9993

Distributed Turbulent Flow Control by Neural-Networked MEMS

F49620-93-1-0332

Principal Investigator

C. M. Ho
Mechanical and Aerospace Engineering Department
University of California, Los Angeles
Los Angeles, California 90095

Phone: 310-825-9993 Fax: 310-206-2302
E-mail: chihming@seas.ucla.edu

Co-Principal Investigators

R. Goodman **J. Kim** **Y. C. Tai**

Introduction

The goal of the URI project is to develop the technologies necessary for monolithically integrating MEMS components with microelectronics to form a truly independent system in which all components necessary for the operation of the system is contained on a single silicon chip. The application chosen to demonstrate this system is the age-old objective of fluid dynamicists to interact with and control the turbulent boundary layer. In the turbulent boundary, structures of very small physical (< 1mm) and time (> 1kHz) scales are prevalent. To interact with and influence these structures requires devices that can match both the physical and time scales. Thus, the ideal candidate is MEMS technology.

To successfully accomplish this task requires the collaboration of the different disciplines involved. The MEMS devices and the techniques with which they can be fabricated had to be developed and the proper manner to employ these devices must be found. The investigators participating in this project consist of researchers in the MEMS, computational fluids, experimental fluids, and electronics areas. The MEMS and electronics groups are responsible for the development of the devices and the necessary driver circuitry. The fluids groups are responsible for finding the most effective application of the devices in order to influence the turbulent boundary layer, and specifically to influence the boundary layer in such a way as to result in a reduction of the shear stress on the surface of a wall.

In the first phase of the URI project, MEMS transducers were developed which can interact with the turbulent boundary layer. A shear stress sensor was developed by Jiang

which proved to be capable of detecting the fluctuations of the shear stress on the surface of a wall. An electromagnetic microflap was developed by Tsao which operates at frequencies of the same time scale as the boundary layer structures. Tung found that the shear stress at the wall could be reduced in direct ratio to the tip velocity of an oscillating microflap. Finally, Lee et al found that a neural network could be effective in determining the optimal control response of suction and blowing system in order to reduce the shear stress. In addition, it was found that a relatively simple input grid was sufficient to make the network effective. Thus, many issues concerning the overall project have already been addressed in the first phase.

In the current phase of the project, the objectives have been to integrate the various components developed in the previous phase and to extend the neural network that Lee employed in his computational study to an actual physical control system. Over the course of the current phase of research, numerous obstacles were overcome. New MEMS devices and fabrication techniques were developed that allowed the formerly incompatible CMOS and MEMS devices to be integrated onto a single chip. Experimentation work revealed and solved many of the problems associated with having electronic devices work in such proximity with each other and is progressing on the efforts to develop a control system using a neural network logic. Implementation of the network developed by Lee, as well as a more general, fully adaptive neural network onto electronic circuitry has been accomplished. The latter implementation allows for actuators which behave differently from the idealized blowing and suction actuators used by Lee in his study. Finally, CFD studies have been performed which reveals and explains the mechanisms at work in the interaction between an oscillating flap and the turbulent boundary layer.

MEMS

The objective of the MEMS part of the project is to develop a system-on-a-chip technology that integrates all distributed shear-stress sensors, magnetic flap actuators and CMOS electronics for turbulent boundary layer flow control. Here we report our successful effort in the following regarding the developed technology.

Shear-stress Sensors:

Technology

We had worked on silicon-nitride-diaphragm shear-stress sensors, but integration of silicon-nitride based sensor was not successful as no foundry could accommodate our process. We have since then changed our strategy and developed a low-temperature post-IC process that produces successful integrated shear-stress sensors. Here, we then present our successful results of the fully integrated constant-temperature hot-wire shear stress sensors (as shown in Fig. 1) that are fabricated on foundry-processed 4″ CMOS wafers.

Due to contamination concerns, no IC foundry, as far as we know, would allow pre-processed wafers to enter their processing line. As a result, we believe the only approach to achieve our goal is to fabricate MEMS devices onto foundry-finished wafers. In such an approach, there could be many limitations on the add-on MEMS processes to ensure they do not damage the functionality of the electronic circuit. One obvious limitation is

on the processing temperature, i.e., all post-IC processes should be below 450°C, which is about the temperature that the aluminum used for electronic connections can withstand. This limitation rules out the application of common MEMS structural materials such as LPCVD silicon nitride and polysilicon that one would like to deposit on the wafer because they are typically deposited above 450°C. Therefore, the structural materials of the previously reported MEMS devices using this approach have mostly been limited to existing CMOS dielectrics, polysilicon and metals, which are not suitable for our use. As a result, we decided to add a new MEMS structure material to the CMOS wafers, while developing other steps to create a vacuum cavity with adequate silicon etching. The new technology uses room-temperature CVD Parylene to build the diaphragm of the shear-stress sensors and the MOSFET gate polysilicon as the sensing element, as described in the following.

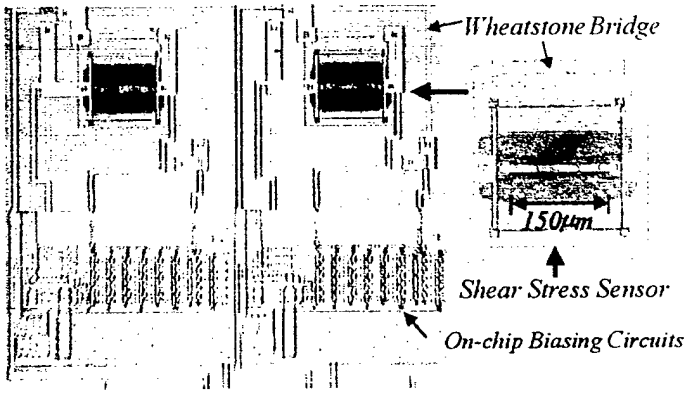

Figure 1: Shear stress sensors integrated with biasing circuit

The fabrication process is shown in Fig.2. First, the CMOS circuitry including the biasing and amplifying circuits for the sensor is fabricated using the MITEL 2μm Double-Poly/Double-Metal CMOS processes. Here, the 3,225 Å thick gate poly (20 Ω/sq, 0.1%/°C TCR) is also used as the hot-wire sensing element, which is on top of the 325 Å gate oxide. The Al layer then serves as the etch-stop for the passivation layer opening. SF_6 plasma etching is adopted to etch away the metal barrier layers and Buffered HF is used to etch away the inter-poly layer and gate oxide layer to expose bulk silicon. A 1-um-thick film of Parylene is then deposited at room temperature and patterned by oxygen plasma etching at 400 mTorr and 400 W. The Parylene plasma etching has loading effects with a non-uniform etching rate of 0.1~0.5 μm/min. In order to keep the etching openings of parylene diaphragm as small as possible for ease of sealing, 4 μm wide slots are opened and overlap with the edge of the sensor bridge. This way, the actual etching slot has a width of about 2 μm. Next, BrF_3 is used to etch the bulk silicon in two to three pulses with each pulse lasting one minute. The second layer of Parylene (2μm) is then deposited for the purpose of etching slot sealing. In the mean time, about 0.5-1μm of Parylene is deposited on the backside of the sensor diaphragm. Finally, oxygen plasma etchback is done with timed etch. Two types of shear-stress sensors are fabricated. Type A has 3.5μm thick Parylene diaphragm over a vacuum-

sealed cavity, while type B is made by etching back of Type A in oxygen plasma, resulting in a 0.7-μm-thick Parylene diaphragm over an air filled cavity. Type A has a deformed diaphragm due to the atmospheric pressure. The maximum deflection is about 5μm, measured by a surface profiler. The trade-off of the vacuum sealing is a thicker and warp-down Parylene diaphragm, which will affect the sensor sensitivity. Therefore, we fabricated another type (Type-B) of sensor by oxygen plasma etchback to eliminate the recess and reduce the diaphragm thickness to the sub-micron level. As a result, this type of sensor (as shown in Fig.2) has an air-filled cavity with a flat diaphragm and has venting holes smaller than the original etching slots.

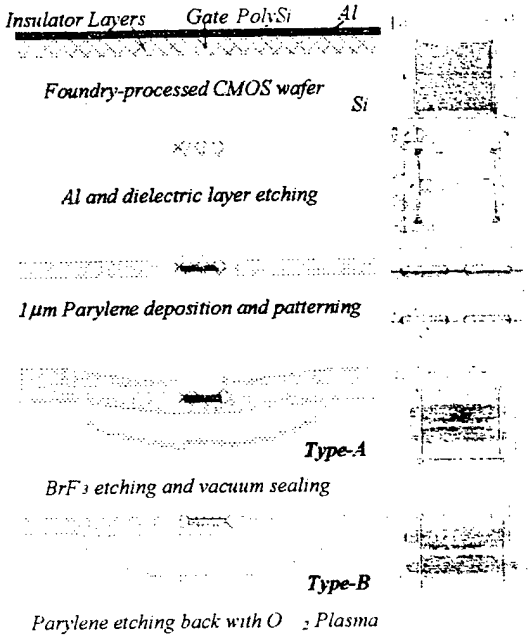

Figure 2: Sensor process technology.

The total power dissipation of a heated wire includes thermal conduction convection and radiation through the wire, the diaphragm, the air and the substrate.

Sensor Calibrations and modeling

The fabricated sensors with their integrated CT circuits are calibrated in a windtunnel with fully developed channel flow. The time-averaged voltage outputs at steady-state flow are calibrated against known wall shear stress levels, which are obtained from the centerline velocity using the following relationship,

$$\tau = 0.00826 R_e^{-0.178} U_\infty^2 \rho$$

Where $R_e = (U_\infty d / \nu)$ is the Reynolds number, d the half height of the windtunnel, ν the kinematic viscosity, ρ the density of air and U_∞ the free stream mean velocity (5-25 m/s). The sensors are packaged on a PC board with a recess in the center so that the chip can be flush-mounted into the wall of the windtunnel. A 6V DC is applied to the integrated chip. The output voltage from the on-chip CT circuit is monitored by a 12bit data acquisition system. Fig.3 shows the typical output voltage against wall shear stress. The device has shown a shear-stress sensitivity of 30 mV/Pa and a bandwidth of 18 kHz.

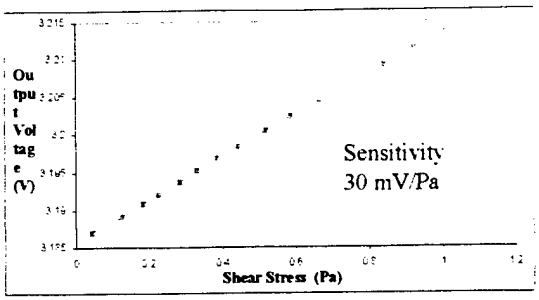

Figure 3: Sensor calibration with a CT circuit.

Interestingly, it has been experimentally observed that our MEMS devices often disagree with the classical hot-wire or hot-film theory, which states that the heat removed by the flow is proportional to the 1/3-power of the shear stress. This suggests that there may be phenomena that the classical theory does not consider, and that a new theory should be developed for the operation of MEMS thermal shear-stress sensors. As a result, we performed a systematic study including both experimental and theoretical investigations to address this issue. By wind-tunnel testing of various designs of MEMS shear-stress sensors with different membrane thickness, size and material, we first obtain experimental data that confirms the inadequacy of the classical hot-wire/hot-film theory. A more thorough theoretical analysis follows, identifying that this invalidity is due to the lack of a thin thermal boundary layer in the flow. Then, a 2-D MEMS shear-stress sensor theory is developed. We show that by incorporating important heat transfer effects that are ignored by the classical theory, the new model provides a closed-form approximate solution and consistently describes all the MEMS sensors. Moreover, we also present 3D heat transfer simulation that agrees with experiments and supports our new 2-D model. This work demonstrates that many classical assumptions made for conventional thermal devices need to be carefully re-examined for miniature MEMS devices.

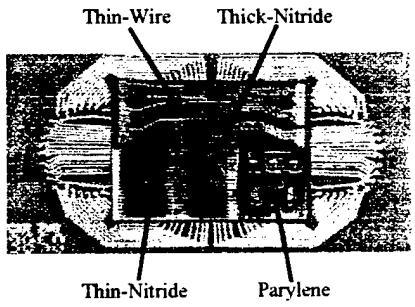

Figure 4: Four MEMS sensors on the same PCB.

We have conducted wind-tunnel experiments with four different MEMS shear-stress sensors. Three of the sensors (Fig. 4) have a polysilicon hot wire on a silicon-nitride membrane. These sensors have membrane thickness and hot-wire width of 1.5 μm and 7 μm (the "thin-nitride" sensor), 3 μm and 7 μm ("thick-nitride"), and 1.5 μm and 3 μm ("thin-wire"), respectively. In the fourth sensor (the "Parylene" sensor), the hot wire (width = 10 μm) is on a Parylene membrane. The polysilicon hot wires in all four sensors

have a thickness of 0.5 μm. These MEMS sensors are carefully placed on a single PC Board (Fig. 4) to ensure uniform testing conditions and consistent testing results. The PCB is then flush-mounted on the inner wall of a 2-D wind-tunnel.

The wind-tunnel testing results are shown in Fig. 5. During sensor operation, the power (denoted P) needed to maintain the hot wire at a constant temperature depends on the wall shear stress (denoted τ). The classical theory states $P\text{-}P_0 \propto \tau^{1/3}$, where $P_0 = P_{|\tau=0}$. However, the significantly curved lines in Fig. 5 clearly indicate that this is not true.

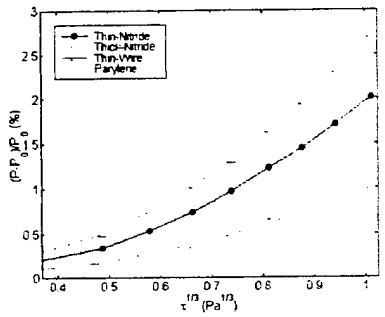

Figure 5: Measured shear-induced power change vs. shear stress$^{1/3}$.

Therefore, we have developed a new theory needs to be developed to consistently describe MEMS sensor operation. Clearly, the new theory must allow a thick thermal boundary layer ($\delta \sim L$). Heat conduction in the membrane is also important, since it can be shown that the abrupt change in the prescribed surface temperature, as assumed in the classical model, is ill-posed in the absence of a thin thermal boundary layer

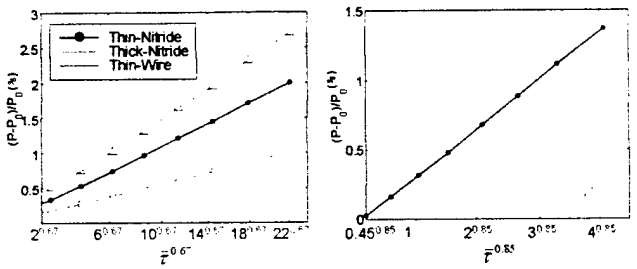

Figure 6 Measured shear-induced power vs. (a) $\tau^{0.67}$ for the nitride sensors (τ = 1 Pa gives $\bar{\tau} \approx 22$), and (b) $\tau^{0.85}$ for the Parylene sensor (τ = 1 Pa gives $\bar{\tau} \approx 4$).

Based on our model, we can alternatively approximate the numerical solution by

$$\Delta\bar{P} = [0.129\lambda^{0.45}/(1+1.81\lambda^{0.55})]\bar{\tau}^{0.85}$$

for $0.6 \le \bar{\tau} \le 5$, and

$$\Delta\bar{P} = [0.187\lambda^{0.5}/(1+2.1\lambda^{0.59})]\bar{\tau}^{0.67}$$

for $2.5 \le \bar{\tau} \le 25$. In both cases, the applicable range of λ is still $0.04 \le \lambda \le 5$ and the approximation error is within 10%, where

$$\bar{\tau} = \frac{\tau L^2}{\mu \alpha}, \qquad \bar{P} = \frac{P}{2k(T_0 - T_\infty)B}, \qquad \text{and} \qquad \lambda = \frac{k_m t}{kL}.$$

We now plot our experimental data in the appropriate range of $\bar{\tau}$ in Fig. 6. It can be seen that the nitride sensors, and the Parylene sensor, indeed approximately follow the 0.67th- and 0.85th-power laws, respectively. This confirms that our 2D theory correctly predicts the trend of MEMS sensor operation.

To summarize, the classical theory for macroscale thermal shear-stress sensors was shown to be invalid. A 2D theory was developed to correctly predict the trend of MEMS sensor operation. The 2D models were both compared with experimental data, and yielded excellent qualitative and quantitative agreement.

Integrated Magnetic Flap Actuators:

We had reported the feasibility study of using torsional microactuators to reduce the shear stress under a turbulent streak. We reported here two sets of wind tunnel experiments. Both used bulk micromachined magnetic flap-type actuators.

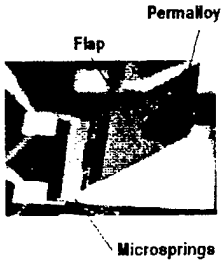

Figure 7: Example of a bulk micromachined flap used in one of the actuator-flow interaction experiments in laminar flow. The flap is 4x4 mm^2.

The first set of experiments was designed to measure actuator-flow interaction in a laminar flow. Because there are no short-lived turbulent structures in this flow, the relatively large (4x4 mm^2) actuators (Fig 7) used were designed to provide large displacements, typically 1 or 2 mm, at low frequencies, typically less than 100 Hz. The conclusive results is shown in Figure 8, which suggests that ωA (angular frequency multiplied by flap deflection, or tip velocity) may be the important control parameter. Figure 9 shows the device and its frequency response.

Based on the results, we have focused on the mechanical and electrical performance characterizations. Magnetic flap actuators have been used in this project since the inception. We use bulk, rather than surface, micromachined processes. The primary reason for this is the desire to achieve a higher operating frequency than previously obtainable (several kHz vs. hundreds of Hz). This higher frequency better matches the lifetimes of the vortical structures (millisecond lifetimes). Using a bulk process allows for the fabrication of thicker beams (tens of microns vs. microns), and thus, a higher resonant frequency.

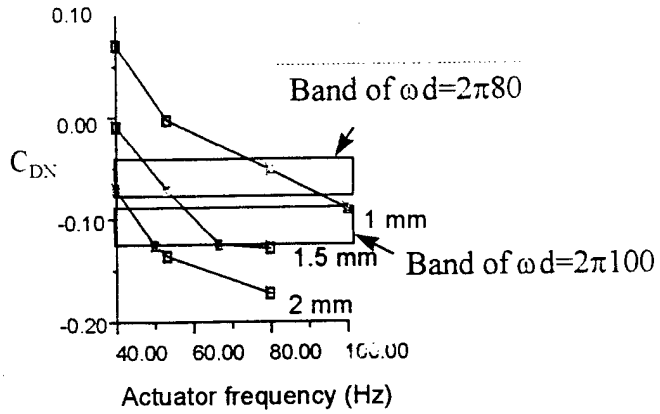

Figure 8. Graph showing (for different amplitudes) drag reduction/increase as a function of frequency. C_{DN} is defined as $(C_d-C_{dl})/C_{dl}$ where C_{dl} is the drag coefficient in a laminar flow. A negative value on the y-axis represents drag reduction. Each curve represents a different amplitude (measured in mm) actuation. Different points with the same value of ωA have approximately the same drag reduction effect.

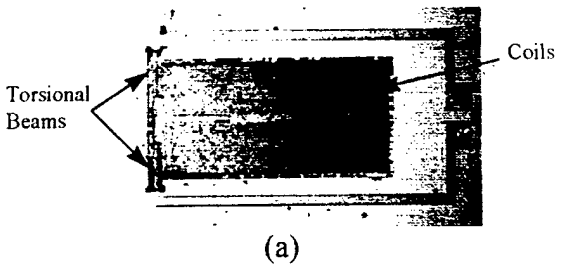

(a)

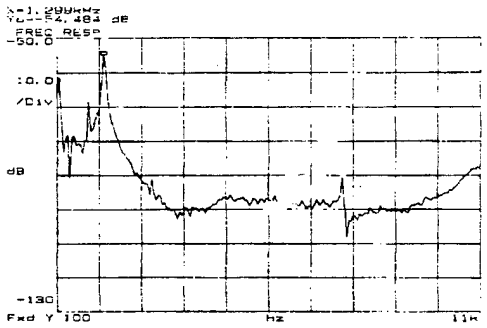

(b)

Fiure 9. (a) Picture of magnetic flap used in actuator-flow interaction testing in fully developed turbulent flow. The flap is 2x1 mm^2. (b) Frequency response of actuator shown in (a). The first order resonant frequency is 1.3 kHz. The higher resonance (7.45 kHz) corresponds to a twisting mode.

Conceptual drawings of the top view and cross sectional view of the actuator are shown below. We initially receive wafers from Mitel, an IC foundry, with aluminum coils and diffused silicon strain gauge over the areas the actuators will be fabricated. Additionally, the wafer contains electronics and sensor elements, whose details are discussed elsewhere. Here, we emphasize the actuator processes. We pattern the backside, and use deep reactive ion etching (DRIE) to etch the silicon until a diaphragm of desired

thickness remains. This remaining thickness can be easily controlled, resulting in the ability to fabricate flaps of different resonant frequencies. Finally, we pattern the front side, then use DRIE again to release the flap. Figure 10 and 11 then shows the design and finished devices. It is important to note that this process is compatible with shear stress sensor fabrication process, which is planned for total integration.

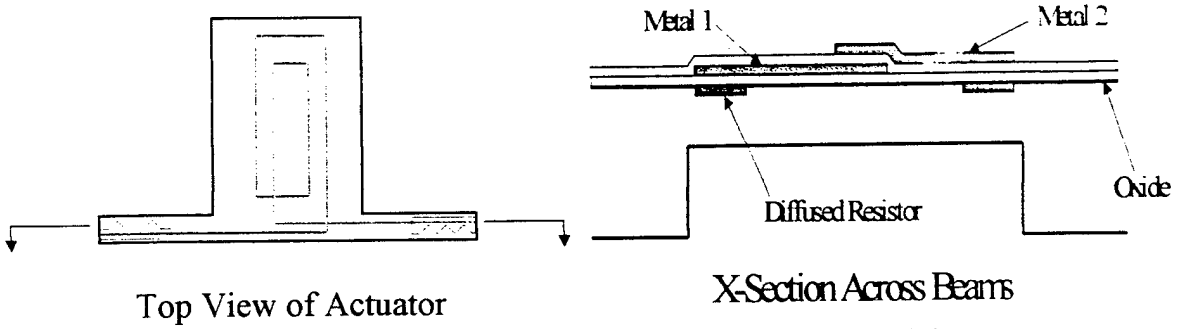

Figure 10: Conceptual drawings of the bulk micromachined magnetic flap actuator.

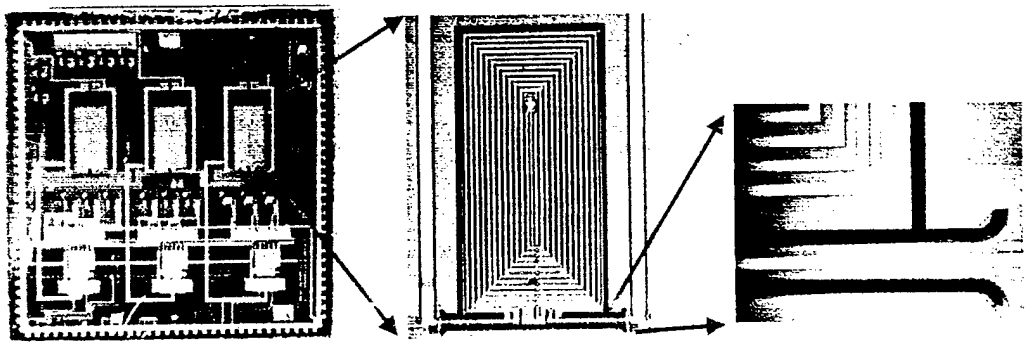

Figure 11: Pictures of the M3 chip (left), magnetic actuator (middle), and a close-up view of the DRIE etch cavity, showing little undercut (right).

The frequency response of the actuator is shown below, which is measured by the laser vibrometer. In order to achieve the largest deflection, the actuator is excited at the first order natural frequency, which is designed to be 3 kHz and measured to be approximately 3.4 kHz. This result is very consistent across many actuators and very close to the calculated expectation, indicating that the DRIE etching process results in a very uniform etch. The deflection amplitude at resonance is measured using an interferometer and is approximately 60um. Additionally, several thinned actuators were also fabricated, and their dynamic response is shown in Figure 12.

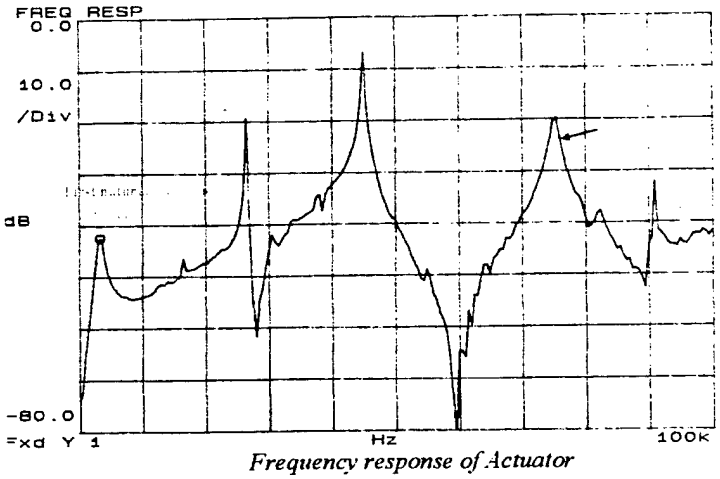

Figure 12. Typical frequency response.

Total Integartion:

Finally, the M^3 chip containing the necessary components to apply turbulence control has been successfully fabricated. This chip comprises of shear stress sensors and microflap actuators and their respective driving circuitry and is shown in Figure 13. Much work has been done to ascertain the functionality of the components, i.e. sensors and actuators. and to characterize these components. Improvements were made to both sensor design and fabrication process to attain better performance.

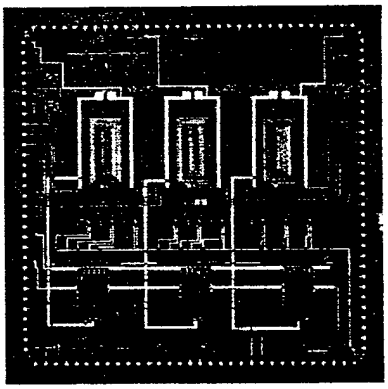

Figure 13 The newly developed M^3 Chip that successfully integrates Parylene shear-stress sensors, magnetic flap actuators and CMOS together.

Experimentation

The experimental efforts of this project have been focused on integrating the technologies and results developed by the other contributors to develop an effective system for applying control to the turbulent boundary layer. As noted earlier, a functional M^3 chip, which successfully integrated working micro-sensors, actuators, and electronics, has already been fabricated. It is the goal of these experimental efforts to develop the control logic which would make this M^3 chip a stand alone control system for the turbulent boundary layer.

In order to develop the control strategy, a real-time feedback control system was assembled using available components. A schematic of the system is shown in Fig. 14. In this system, an upstream sensor array measures the incoming flow and sends the signals to the processing computer. In turn, the computer calculates a control response based on a neural network control logic and sends it to the actuator. The downstream sensor array detects the effects of the application of control. This system has been shown to be capable of operating at speeds in excess of 8 kHz.

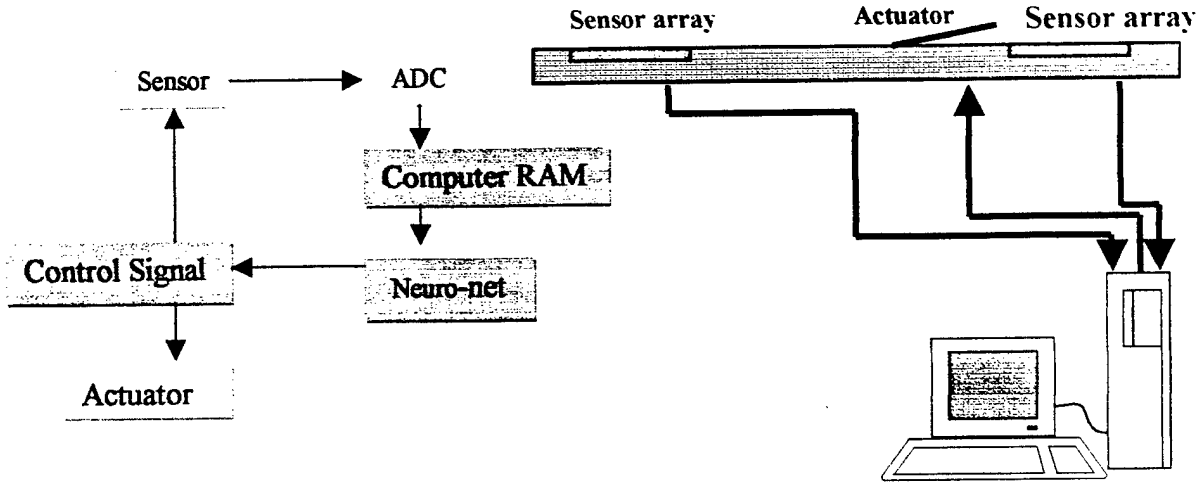

Figures 14a and 14b: Real-time control process diagram and system setup

The sensor array used is one developed by Jiang for the first phase of this project. Much has been written about this sensor and its performance has been verified. A picture of the sensor array is shown in Fig. 15.

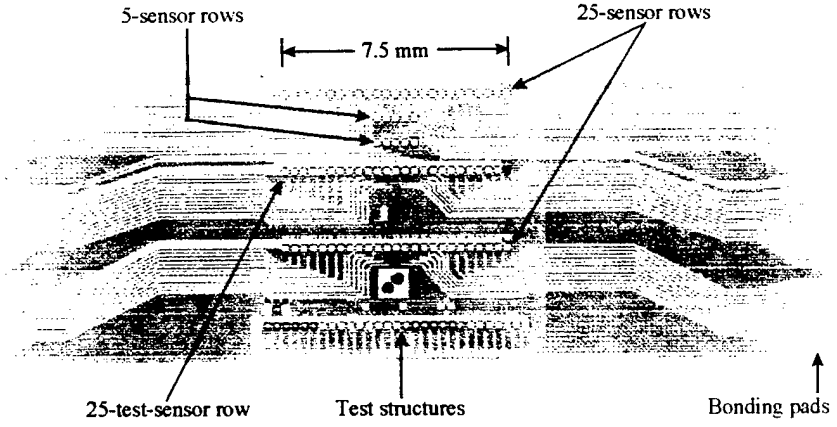

Figure 15: The micromachined shear stress sensor array with over 100 sensors

The actuator used is the microflap found on the M^3 chip. Since the microflap is a newly developed component, much characterization work had to be done. By design, the flap actuates at a significant level only at its resonant frequency, about 3.5 kHz in most instances. The response of the flap, under no aerodynamic loading, due to a continuous and a discreet driving signal is shown in Fig. 16. The driving power to the flap is approximately .8 W. The measurements were made using a commercial deflection meter.

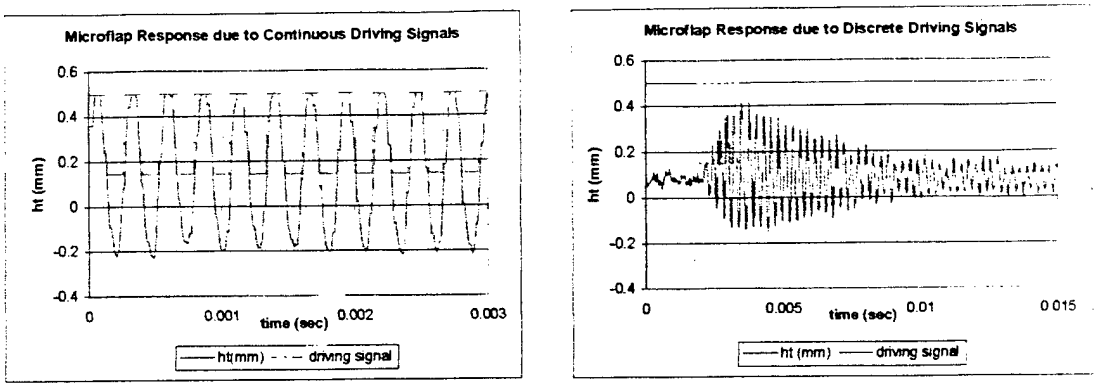

Figure 16: Microflap response due to continuous and discreet driving signals

In order to measure the flap deflection under operating conditions, a different method had to be employed, as the geometry of the wind-tunnel precluded the use of the deflection meter. Instead, the light lever principle was applied, in which a laser beam was reflected off the flap and onto a position sensitive detector. By locating the beam on the detector, the deflection height and angle can be calculated. The schematic of the set-up is shown in Fig. 17. The adjacent table shows the driving power to the flap and the corresponding deflection height and tip velocity. The measurements are taken while the flap is under loading from a 10 m/s flow.

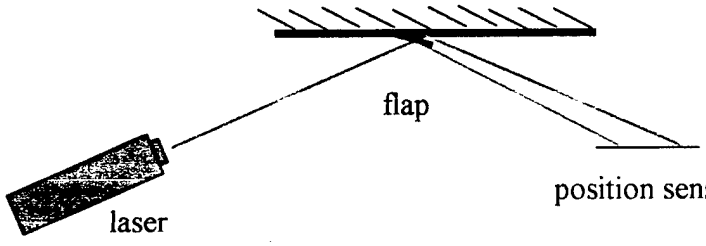

Power (watt)	0.1	0.049	0.025
Deflection (mm)	0.01	0.009	0.007
Velocity (m/s)	0.2	0.18	0.14

Figure 17: Setup for measurement of microflap deflection height

One of the obstacles which had to be overcome in assembling the control system is the issue of heat generation by the microflap. Temperature measurements on the M^3 chip surface showed that the temperature can reach as high as 160 deg. C. This heat reaches the shear stress sensor array both by convection by the airflow and conduction from the M^3 chip itself. A picture of the actual sensor-actuator set-up is shown in Fig. 18. As can be seen, the sensor array chip is actually in contact with the M^3 chip, the heat source, thus exasperating the heat transfer problem.

The solution to this problem was to transform one of the shear stress sensors into a temperature through use of a low overheat, constant current circuit. By locally measuring the temperature in the proximity of the shear stress sensors, the heating effects of the microflap can be compensated.

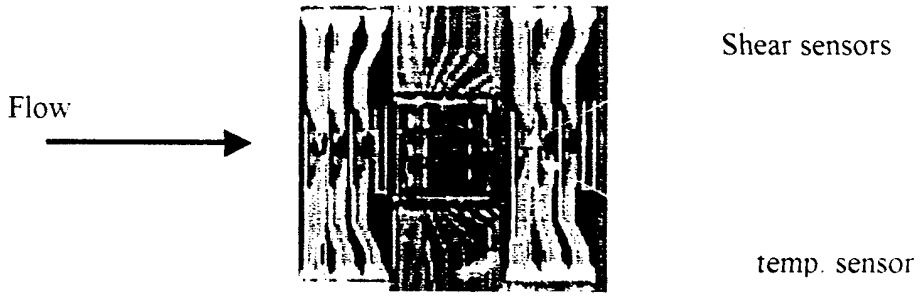

Figure 18: Orientation of sensor array chip to M^3 chip

A second obstacle comes from the electronic noise generated by the driving signals to the microflap. In a basic application of Faraday's Law, the time varying voltages used to drive the microflap induces a voltage change in the shear stress and temperature sensors. This problem was further exasperated by the large gain (over 5,000 times) applied to the temperature signals. As a result, measurements showed a misleading oscillation at the same frequency of as the driving signal to the microflap. Much experimentation had to be done in order properly to shield the system and minimize this noise. The raw temperature signal with and without shielding is shown in Fig. 19 (please note that the signals were recorded at different gains).

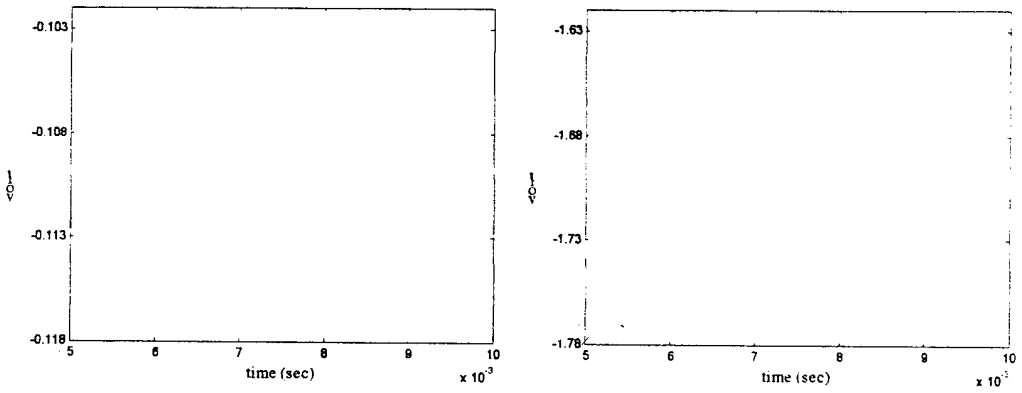

Figure 19: Temperature sensor signal with and without shielding

The resolution of these problems allows the work determine the control logic to progress once again. The goal is to implement a neural network which can determine the appropriate actuator response given the flow measurements. This network will most likely be based on one that was developed by previous CFD work. A version of this network, which showed itself capable of predicting the incoming streamwise shear stress field based on the current measurements, has already been implemented. A block diagram of this network is shown in Fig. 20, along with the prediction results as compared with the actual measurements. The first 7 weights are applied to the measurements from 7 spanwise sensors. Weights 8 and 9 are applied to temporal records of the central sensor at 1 and 2 sampling time steps prior to the current one, respectively. The network then predicts the sum of the streamwise shear stress as some later time. The prediction results shown are for the shear stress at two time steps after the measured values (note: the sampling rate was at 3.2 kHz). As can be seen, the calculated values

very closely track the actual measurements, with the exceptions being at the extreme peaks. This success gives great encouragement that a neural network will be capable of determining an effective control logic.

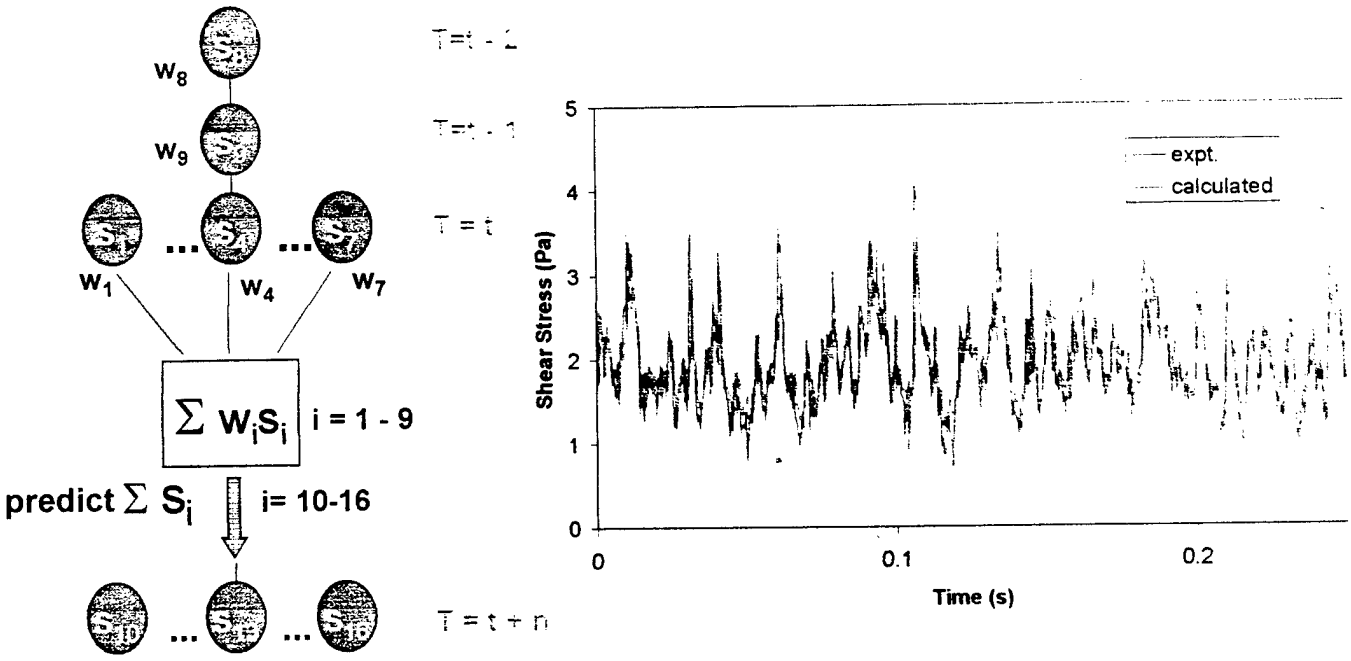

Figure 20: Block diagram of neural network used in experiments and corresponding prediction results

Neural Network Circuits

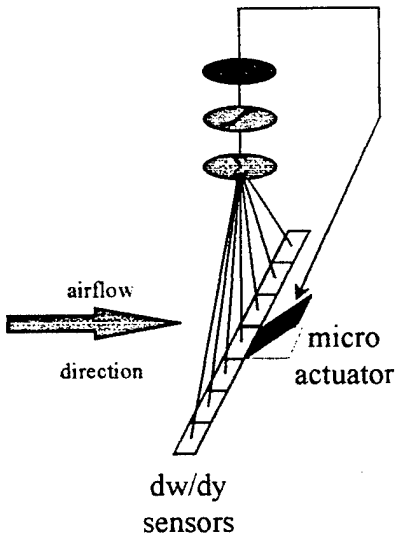

Figure 21

Previous neural network training led to the development of a control law of the form:

$$\upsilon_{jk} = C\sum_{i=-3}^{3} W_i \frac{\partial w}{\partial y}\bigg|_{j,k-i} \quad , \quad C = \frac{K}{\sqrt{\sum_j \upsilon_j^2}}$$

Where υ_{jk} are velocity outputs, the W_i are fixed weights, and C is chosen such that the root-mean-squared value of the actuation is kept at $0.15u_\tau$. In hardware (figure 21), we wimplement a single row of $\partial w/\partial y$ sensors that trigger a single row of actuators. The first thing that must be accomplished is the summing and weighting of the sensor output voltages for $\partial w/\partial y$. The circuit in Fig. 22 is used for this purpose.

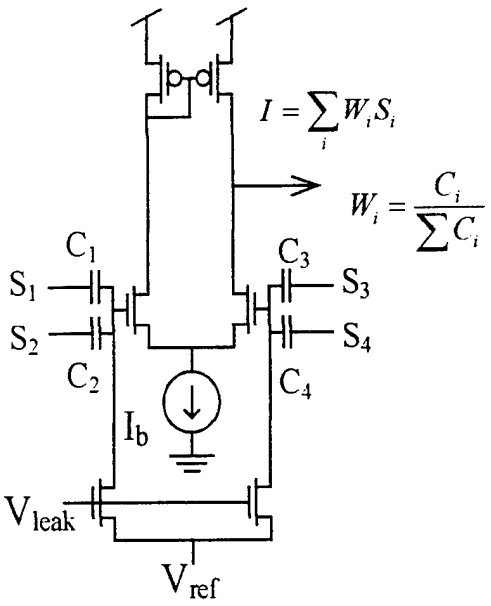

Figure 22. Summing and weighting circuit

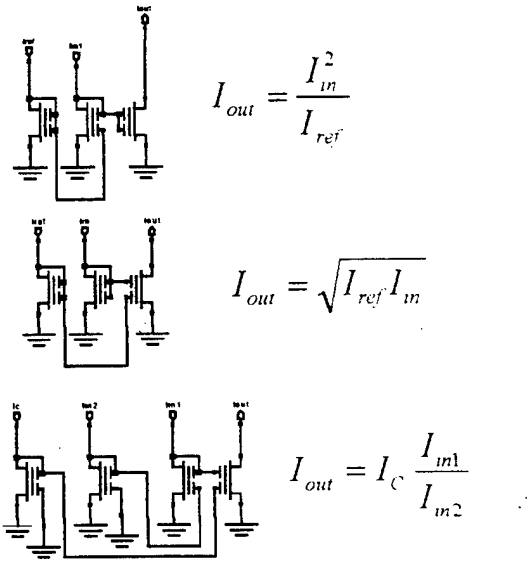

Figure 23. Building blocks of RMS circuit

The weight pattern can be implemented by choosing the capacitor ratios to match the fixed weight pattern for W_j obtained from the neural network training. Next, the output of the weighting and summing network is to be scaled and normalized by the RMS value of the other sensor arrays. The building blocks of the RMS circuit are shown in Fig. 23. These building blocks are placed together to provide the rms normalization and scaling circuit.

Figures 24 and 25 show the test results from the weighted summation circuit and the normalization circuit. The lines represent the ideal theoretical fits and the symbols are the actual data. Both circuits show very good performance.

These circuits form the core of the signal processing circuitry for the control law implementation. The output of the normalization circuit goes to a current amplifier to drive the actuators. The circuits are all analog and perform all of the computations in real time.

These circuits were based on neural network training with idealized sensors and actuators. Unfortunately, it was discovered that the actual flap actuators may exhibit

characteristics which are quite different from the idealized blowing and suction actuators. Thus, it was decided that a more general, fully adaptive neural network circuit would be necessary.

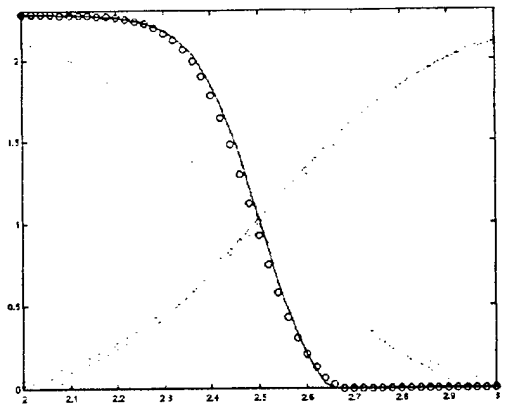

Figure 24. Weighted sum circuit test results

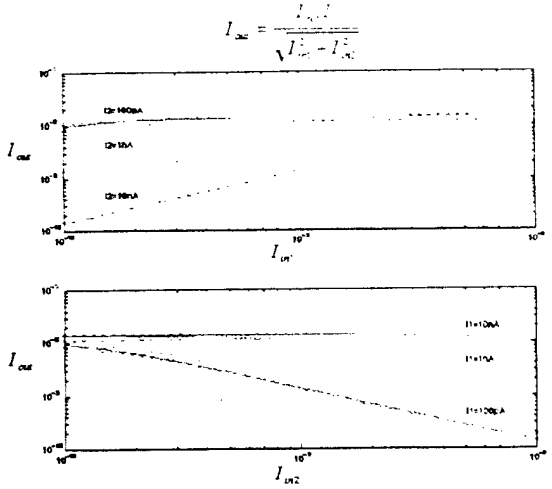

Figure 25. RMS norm. circuit test results

There are several issues that must be addressed in the implementation of an analog VLSI neural network chip. First, an appropriate algorithm suitable for VLSI implementation must be found. Traditional error backpropagation approaches for neural network training require too many bits of floating point precision to implement efficiently in an analog VLSI chip. Techniques that are more suitable involve stochastic weight perturbation, where a weight is perturbed in a random direction, its effect on the error is determined and the perturbation is kept if the error was reduced; otherwise, the old weight is restored. In this approach, the network observes the gradient rather than actually computing it. In general, however, the gradient descent techniques converge more rapidly than the perturbative techniques.

Next, the issue of how to appropriately store the weights on-chip in a non-volatile manner must be addressed. If the weights are simply stored as charge on a capacitor, they will ultimately decay due to parasitic conductance paths. One method would be to use an analog memory cell currently being developed. This would allow directly storing the analog voltage value. However, this technique requires using large voltages to obtain tunneling and injection through the gate oxide and is still being investigated. Another approach would be to use traditional digital storage with EEPROM's. This would then require having A/D/A (one A/D and one D/A) converters for the weights. A single A/D/A converter would only allow a serial weight perturbation scheme that would be slow. A parallel scheme, which would perturb all weights at once, would require one A/D/A per weight. This would be faster, but would require more area. One alternative would remove the A/D requirement by replacing it with a digital counter to adjust the weight values. This would then require one digital counter and one D/A per weight.

A small synapse with one D/A per weight has been achieved by first making a binary weighted current source and then feeding the voltages that correspond to those currents to mirrored transistors on the synapse. Thus, we achieve many D/A's with only one binary

weighted array of transistors. Figure 26 is an example of such a synapse. The synapse performs the weighting of the inputs by multiplying the input voltages by a weight stored in a digital word denoted by b0 through b5. The sign bit, b5, changes the direction of current to achieve the appropriate sign. The synapse circuit outputs a differential current that will be summed in the neuron circuit shown in Figure 27. The neuron circuit performs the summation from all of the input synapses. The neuron circuit then converts the currents back into a differential voltage feeding into the next layer of synapses.

Using these two circuit building blocks it is possible to construct a multilayer feed-forward neural network. The nonlinear squashing function is actually performed in the synapse circuit rather than in the neuron as in a traditional neural network. However, this is equivalent as long as the inputs to the first layer are kept within the linear range of the synapses.

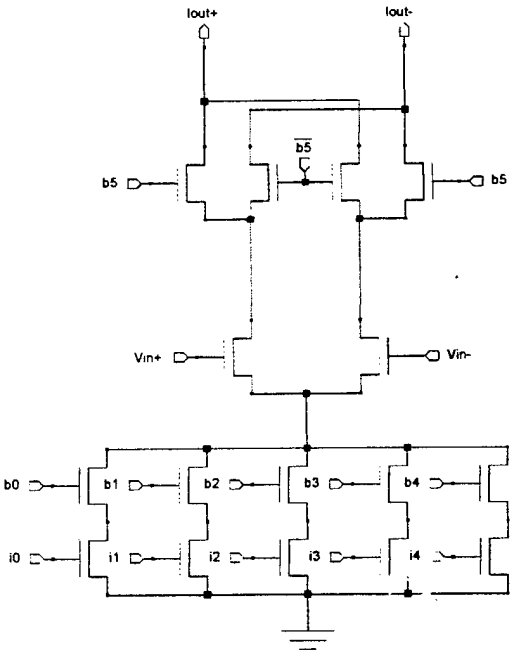

$$\Delta I_{out} \approx \text{sigmoid}(I_{weight} \Delta V_{in})$$

Figure 26. Synapse Circuit

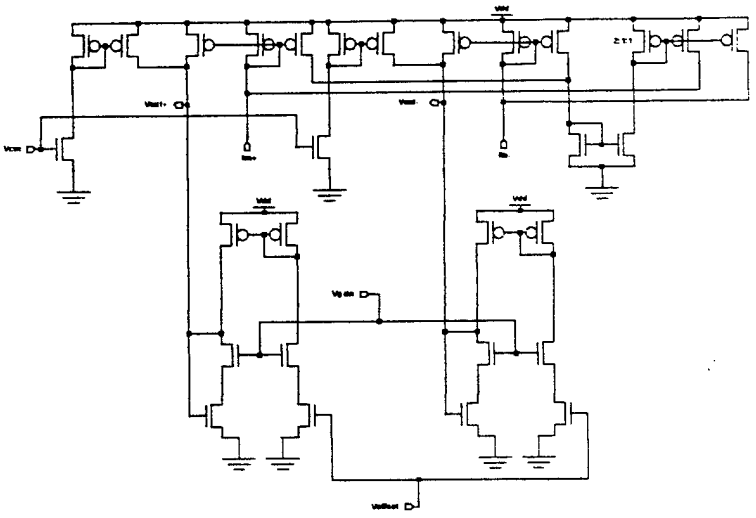

$$\Delta V_{out} \approx R \Delta I_{in} = R \left(\sum_i \left(I_{weight_i} \Delta V_{in_i} \right) \right)$$

$$\text{where } R \approx \frac{1}{2K(V_{gain} - V_T)}$$

Figure 27. Neuron Circuit

The neural network is trained by using the perturbative weight update rule. The perturbative technique requires generating random weight increments to adjust the weights during each iteration. A conceptually simple technique of generating random perturbations would be to amplify the thermal noise of a diode or resistor. Unfortunately, the extremely large value of gain required for the amplifier makes the amplifier susceptible to crosstalk. Any noise generated from neighboring circuits would also get amplified. Since some of this noise may come from clocked digital sections, the noise would become very regular, and would likely lead to oscillations rather than the uncorrelated noise sources that we desire. Therefore, another technique is required. Instead, the random weight increments are generated with linear feedback shift registers

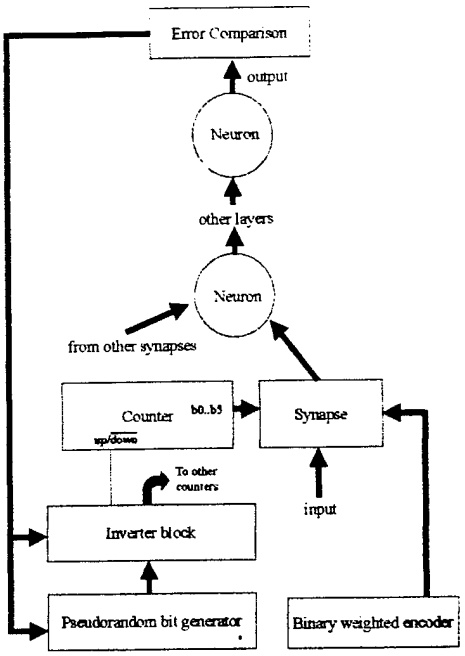

Figure 28. Neural Net Block Diagram

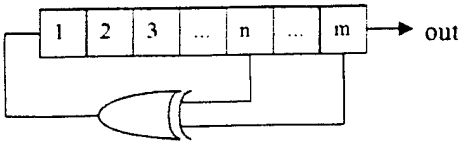

Figure 29. Linear Feedback Shift Register

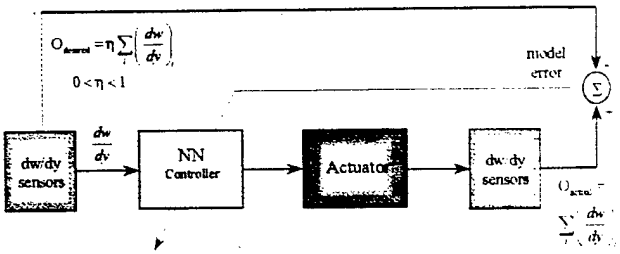

Figure 30. Direct Perturbative Control Scheme

(Figure 29) that produce a long pseudo-random bit sequence. These random bits are used as inputs to a counter that stores and updates the weight. The counter outputs go directly to the D/A converter inputs of the synapses. If the weight updates led to a reduction in error, the update is kept. Otherwise, an inverter block is activated which inverts the counter inputs. This has the effect of restoring the original weights. A block diagram of the full neural network circuit function is provided in Figure 28.

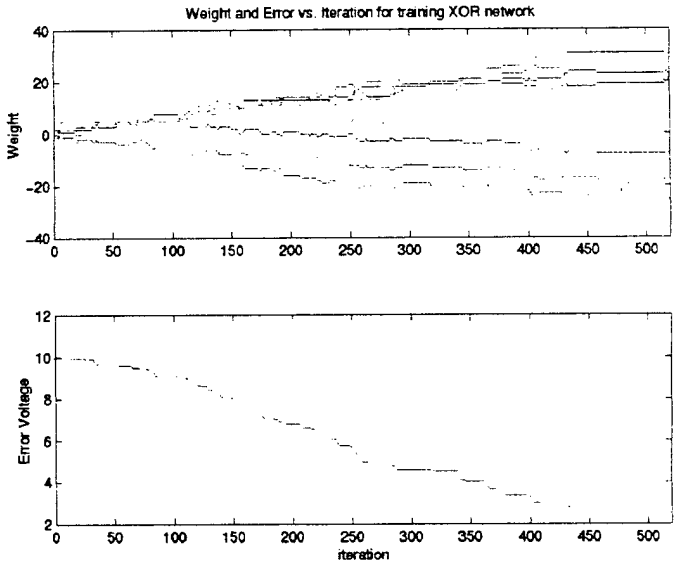

Figure 31. Neural Network XOR Training Run

The above neural network circuits were trained with some simple digital functions such as AND and XOR. The results of an XOR training run is shown in Figure 31. As can be seen from the graphs, the network weights slowly converge to a correct solution.

The network will be used for training with wind tunnel sensor measurements. The final goal is to use the chip for direct perturbative control in the wind tunnel (Figure 30). In this scheme, inputs from upstream sensors go through the neural network to control the actuator. Downstream sensors are used to determine the effect of the actuator. If the drag decreases, the weight perturbation is kept, otherwise it is thrown away. This should lead to a gradual decrease in drag.

Numerical Simulation of Micro-flaps

Although we have developed several control algorithms utilizing various different approaches (e.g., opposition control, neural network, suboptimal control, systems theory) during the course of this grant, all of these control algorithms used surface blowing and suction as control input. Such actuation is simple to implement in numerical experiments, but precise control of blowing and suction in practice in the same manner as implemented in the numerical experiments is difficult to achieve. In order to develop a control strategy for currently available actuators such as micro-flap actuators, development of a new numerical approach, known as an immersed-boundary approach, has been developed and implemented. A brief description of the method is given below.

It was our desire to simulate flow over a complex boundary while retaining the simplicity and efficiency of computation in a Cartesian system. This was done through use of an immersed boundary method. The equations of fluid motion are calculated on the regular geometry of a periodic channel. Insertion of a micro-flap into the flow domain creates an internal boundary, which must be simulated properly. We used an idea of Peskin and McQueen (1989) of using a body force to represent the dynamical effect on the fluid of a moving wall immersed in the fluid. In their method, and our application, the position of the internal boundary within the flow domain does not generally coincide with the computational mesh. Flow properties are interpolated from the computational mesh to the locations of boundary nodes in order to calculate the force of the boundary on the fluid. Then that force is distributed onto nodes of the computational mesh near the internal boundary.

The force in Peskin and McQueen's work was based on a balance of tension in an elastic wall against the hydrodynamic forces. We instead used an idea developed by Mohd-Yusof (1997) of creating a fictitious force constructed so as to drive the velocity at desired locations to desired values. In Mohd-Yusof's application, the desired locations are a riblet surface and the desired values are zero to fulfill the no-slip condition. In our application, the desired locations are the flap positions and the desired values are the flap velocities, also to fulfill the no-slip condition. A difference between Mohd-Yusof's application and ours is the moving boundary created by the flap. Another difference is that the flap is an internal boundary with flow on both sides. Mohd-Yusof's riblet surface is an external boundary with only one side within the flow domain.

The Navier-Stokes equation with a forcing term is temporally discretized to yield,

$$\frac{\mathbf{u}^{n-1}-\mathbf{u}^{n}}{\Delta t}+\mathbf{u}\cdot\nabla\mathbf{u}=-\nabla p+\nu\nabla^{2}\mathbf{u}+\mathbf{f}.$$

In a neighborhood of the flow boundary, we already know what we want the velocity to be at the end of the time step,

$$\mathbf{u}^{n-1}=\mathbf{w}, \tag{2}$$

so we solve for the body force that would bring that velocity about

$$\mathbf{f}=\frac{\mathbf{w}-\mathbf{u}^{n}}{\Delta t}+\mathbf{u}\cdot\nabla\mathbf{u}+\nabla p-\nu\nabla^{2}\mathbf{u}. \tag{3}$$

The body force is applied at two sets of points, those just below the immersed boundary and those just above. Where the boundary coincides with the grid the body force is applied at the boundary and at the points just below it. Application of the force at additional points, particularly below the immersed boundary, was tested but found to give no benefit. Our method of applying the body force gives flexibility in choosing the immersed boundary not found in some other methods, since there is no need to line up the boundary with a grid.

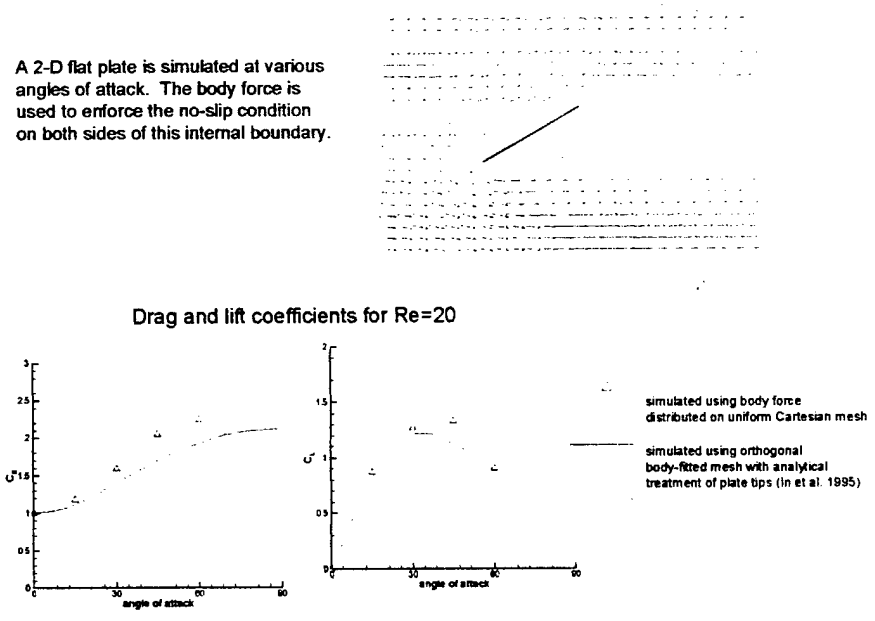

Figure 32: Validation of the present immersed-boundary method

As a validation of the immersed-boundary method, computation of a low-Reynolds number flow over an inclined flat plate was carried out and the results were compared

with those obtained from a conventional calculation as shown in figure 32. The computed drag and lift coefficients were in good agreement, especially at low angles of attack. This simulation method has been useful for examining the interaction of the MEMS actuator with the fluid. Velocity data in the wind tunnel experiments was gathered at discrete stations downstream from the micro-flap. Data resolution is high in the spanwise and wall-normal directions, but not in the streamwise direction. The numerical simulations make data at any point in the flow available for interrogation. The ability to fill in the gaps of the wind tunnel data has helped explain the operation of the actuator. Wind tunnel data showed the flap causing fluid to move away from the wall at a velocity four times faster than the flap itself. There was some question as to whether this could be correct. The numerical simulation produced similar results and provided an explanation. Movement of the flap into higher speed fluid, combined with sucking fluid under the opening flap, created a shear layer, which would roll up into a vortex behind the flap and eject fluid away from the wall. This ejected fluid moved away from the wall much faster than deflection alone could produce. This observation is useful for a couple of reasons. First, it shows the mechanisms whereby the micro-flap can be most effective in influencing the flow. Second, it shows that a flap's actuation will be felt most strongly not at the flap itself, but instead, a short distance downstream.

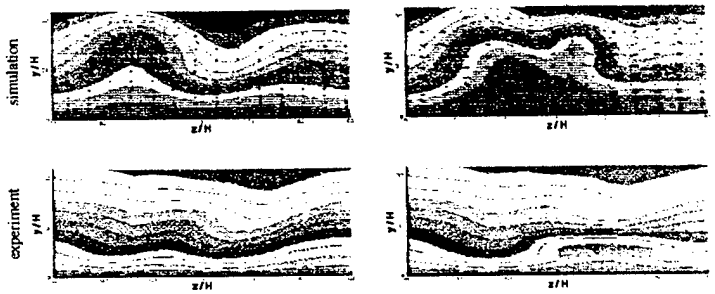

Figure 33: Contours of streamwise velocity in a spanwise-wall-normal plane, one flap-length downstream from the flap

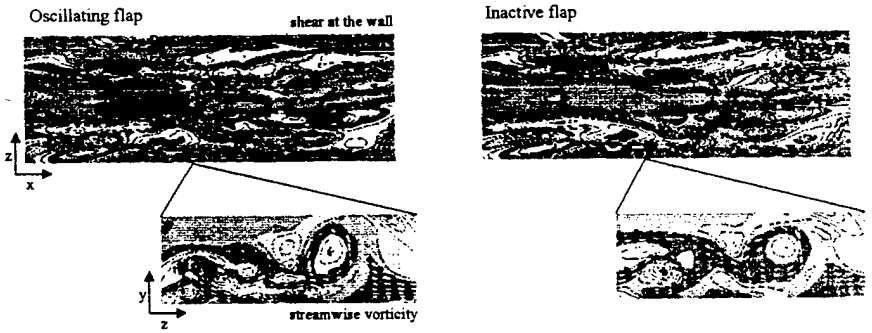

Figure 34: Interaction between a micro-flap and turbulent structures

Laminar flow with a streamwise vortex passing over the flap was generated in the wind tunnel experiments. This was meant to be a simplified analog for the coherent structures found near the wall in a boundary layer. The vortex pulls high-speed fluid close to the wall and generates a high shear region at the wall. This is similar to the sweep events in turbulent boundary layers. The micro-flap actuator counteracts the action of the streamwise vortex and reduces shear at the wall in a region downstream from the flap.

Our numerical simulations give results similar to those from the wind tunnel (figure 33), thus adding further confidence in the immersed-boundary method in handling micro-flaps.

Development of the immersed-boundary method for simulation of a turbulent flow with micro-flaps has not been completed yet. A preliminary result showing the interaction between a micro-flap and near-wall turbulence structures are shown in figure 34. Qualitative comparisons between numerical and experimental results have been strong and encouraging. Quantitative comparisons are currently underway, and when successfully completed will provide a strong validation of using our body force formulation as a model for the micro-flaps. We believe that the immersed-boundary approach is an efficient and cost-effective approach to simulate turbulent flows involving complex geometry. We anticipate that the immersed-boundary method will emerge as a powerful tool for simulating many turbulent flows.

List of Publications:

Kim, J., "Active control of turbulent boundary layers for drag reduction," IUTAM Symposium on Mechancis of Passive and Active Flow Control (eds. Meier and Viswanath), Kluwer Academic Publishers, 1999.

Lee, C., Kim, J. and Choi, H., "Suboptimal control of turbulent channel flow for drag reduction," *J. Fluid Mech.*, 358, 1998.

Tsao, T., F. Jiang, C. Liu, R. Miller, S. Tung, J. Huang, B. Gupta, D. Babcock, C. Lee, Y. Tai, C. Ho, J. Kim and R. Goodman, "MEMS-based active drag reduction in turbulent boundary layers,"
Microengineering Aerospace Systems (ed. H. Helvajian), The Aerospace Press, 1999.

T. Tsao, F. Jiang, R. A. Miller, Y. C. Tai, B. Gupta, R. Goodman, S. Tung, and C. M. Ho, "An Integrated MEMS System for Turbulent Boundary Layer Control," *Technical Digest, 1997 International Conference on Solid-State Sensors and Actuators (Transducers '97)*, Chicago, IL, Vol. 1, pp. 315-318, Jun. 16-19 (1997).

X.Q. Wang, Z. Han, F. Jiang, T. Tsao, Q. Lin, Y.C. Tai, V. Koosh, R. Goodman, J. Lew and C.M. Ho," A Fully Integrated Shear Stress Sensor," *1999 International Conference on Solid-State Sensors and Actuators (Transducers '99)*, Sendai, Japan, Jun.(1999).

Q. Lin, F. Jiang, XQ Wang, Z. Han, Y.C. Tai, J. Lew and C.M. Ho, "MEMS Thermal Shear-Stress Sensors: Experiments, Theory and Modeling," Technical Digest, Solid State Sensor and actuator Workshop, Hilton Head Island, South Carolina, pp. 304-307, June 2000.

V. Koosh, R. Goodman, "VLSI Neural Network with Digital Weights and Analog Multipliers", accepted to 2001 IEEE International Symposium on Circuits and

Systems, May 6-9, 2001

V. Koosh, R. Goodman, "Dynamic Charge Restoration of Floating Gate Subthreshold MOS Translinear Circuits", accepted to 19th Conference on Advanced Research in VLSI, March 14-16, 2001

V. Koosh, B. Gupta, D. Babcock, R. Goodman, F. Jiang, Y.C. Tai, S. Tung and C. M. Ho, "Analog VLSI System for Active Drag Reduction" in G. Cauwenberghs and M. Bayoumi, Eds., Learning on Silicon, Norwell, MA: Kluwer Academic, 1999, Chapter 4